Isobe et al. *NPG Asia Materials* (2020) 12:80
https://doi.org/10.1038/s41427-020-00266-9

NPG Asia Materials

ARTICLE Open Access

Negative thermal expansion in α-$Zr_2SP_2O_{12}$ based on phase transition- and framework-type mechanisms

Toshihiro Isobe[1], Yuko Hayakawa[1], Yuri Adachi[1], Ryosuke Uehara[1], Sachiko Matsushita[1] and Akira Nakajima[1]

Abstract

Materials with negative coefficients of thermal expansion (CTEs) can be used to prepare composites with specific CTE values. Negative thermal expansion behavior can be primarily attributed to two types of mechanisms: phase transition- and framework-type mechanisms. This paper reports $Zr_2SP_2O_{12}$, which has unique negative thermal expansion behavior involving both mechanisms. $Zr_2SP_2O_{12}$ undergoes a framework-type mechanism at temperatures <393 K or >453 K and an isosymmetric phase transition at 393–453 K. The volumetric CTE of α-$Zr_2SP_2O_{12}$ is ~−70 p.p.m./K during the isosymmetric phase transition, and this value can be decreased by decreasing the proportion of sulfur. The minimum volumetric CTE of α-$Zr_2S_{0.9}P_2O_{12-\delta}$ is ~−108 p.p.m./K in the temperature range of 393–453 K. Between 303 and 773 K, the volume of α-$Zr_2S_{0.9}P_2O_{12-\delta}$ is reduced by ~1.3%. Finally, this paper presents methods for the hydrothermal synthesis of α-$Zr_2SP_2O_{12}$ and for controlling the sulfur content.

Introduction

Materials with negative coefficients of thermal expansion (CTEs) are useful for preparing composites with controllable thermal expansion behaviors. The mechanisms active in these materials with negative CTEs can be classified into three categories: atomic radius contraction, magneto-volume effect, and framework-type mechanisms[1–7]. Atomic radius contraction and the magneto-volume effect are often combined into phase transition-type mechanisms; phase transition-type materials have large negative CTEs but narrow usable temperature ranges. That is, the CTEs of these materials are positive at temperatures outside the temperature range of the phase transition, while they exhibit excellent performance within the temperature range of the phase transition[8]. These thermal properties might lead to problems when composites containing phase transition-type negative CTE fillers are exposed to unexpected temperatures. On the other hand, framework-type materials tend to show thermal shrinkage over a wide temperature range and have small absolute CTE values[6]. These materials are usable over a wide temperature range. However, a large amount of framework-type material must be mixed into the matrix to decrease the CTE of the composite[9–11]. Thus, phase transition- and framework-type materials have tradeoffs in terms of the application temperature range and their CTE. Materials able to undergo both types of mechanisms have never been reported.

$A_2M_3O_{12}$-type materials have a negative CTE originating from a framework-type mechanism[12–18], with $Y_2W_3O_{12}$ exhibiting the lowest CTE among $A_2M_3O_{12}$-type compounds[17]. $A_2M_3O_{12}$ can be described as $A_2(MO_4)_3$, indicating two cations and three oxoanions. In this case, $A_2(MO_4)_3$ may also be composed of a plurality of oxoanions with a suitable cation A [e.g., $Zr_2(WO_4)(PO_4)_2$ and $Zr_2(MoO_4)(PO_4)_2$][18]. $NaZr_2(PO_4)_3$ has a similar chemical formula; however, it has a different space group, $R\bar{3}c$. The CTE found for the Na superionic conductor (NASICON) structure based on $NaZr_2(PO_4)_3$ ranges from ~−5 to 5 p.p.m./K[19]. We focused on α-$Zr_2SP_2O_{12}$ with the NASICON structure. α-$Zr_2SP_2O_{12}$ is

Correspondence: Toshihiro Isobe (isobe.t.ad@m.titech.ac.jp)
[1]Department of Materials Science and Engineering, Tokyo Institute of Technology, Tokyo, Japan

known to form when zirconium phosphate gel, an ion absorber, reacts with sulfuric acid[20]. However, the material properties of α-$Zr_2SP_2O_{12}$ have never been reported. In this study, we established a method for synthesizing α-$Zr_2SP_2O_{12}$ and evaluated its CTE using powder X-ray diffraction (PXRD). As discussed in this paper, the synthesized α-$Zr_2SP_2O_{12}$ exhibits unique thermal expansion behavior.

Materials and methods

Sample preparation

$(NH_4)H_2PO_4$ (Fujifilm Wako Pure Chemical Corp., Japan), $ZrOCl_2{\cdot}8H_2O$ (Fujifilm Wako Pure Chemical Corp., Japan), and excess H_2SO_4 (Fujifilm Wako Pure Chemical Corp., Japan) were dissolved in deionized purified water. The obtained precursor was sealed in an autoclave and reacted hydrothermally at 283–453 K for 2–7 days. The resulting product was dried at 573 K for 12 h and then calcinated at 673–1173 K for 4 h in air.

Characterization

PXRD patterns were collected at 303–773 K using a Mini Flex 600 diffractometer (Rigaku, Japan) equipped with a Cu*K*α radiation source. The crystal structure parameters were refined by Rietveld analysis using the RIETAN-FP program[21]. The obtained atomic coordination was visualized, and the bond lengths and angles were measured using VESTA 3. The particle morphology was observed by field emission scanning electron microscopy (FE-SEM) (JSM-7500F, JEOL, Japan). The chemical composition was estimated by inductively coupled plasma atomic emission spectroscopy (ICP-OES; 5100 VDV, Agilent Technologies, USA). Stock solutions (100 mg/L) of zirconium, sulfur, and phosphorus (Fujifilm Wako Pure Chemical Corp., Japan) were used to produce standards for the ICP-OES calibration curves. The obtained powders were dissolved in an acid mixture containing 0.5% HF and 5% HNO_3. Differential scanning calorimetry (DSC; DSC-8230, Rigaku, Tokyo, Japan) of the sample was conducted at 300–773 K (heating rate, 10 K/min) in the air.

Results

Synthesis of α-$Zr_2S_xP_2O_{12-\delta}$

The crystal structure of α-$Zr_2SP_2O_{12}$ includes a corner-sharing ZrO_6 octahedral unit and PO_4 or SO_4 tetrahedral units, as shown in Fig. 1a. This crystal structure was previously reported and indexed as hexagonal[20]. However, the material properties of α-$Zr_2SP_2O_{12}$ have not been previously studied; α-$Zr_2SP_2O_{12}$ has only been reported as a product formed by the absorption of sulfuric acid by zirconium phosphate gel. The synthetic method developed for producing high-purity α-$Zr_2SP_2O_{12}$ was based on the hydrothermal synthetic method for $Zr_2WP_2O_{12}$[22,23]. Fine α-$Zr_2SP_2O_{12}$ was synthesized by heating following the hydrothermal treatment of co-precipitates. The optimum conditions for heating and hydrothermal treatment were evaluated in this study since the temperature and duration of hydrothermal treatment affect the crystallinity of the final product. The optimal hydrothermal treatment temperature and time were determined to be 453 K and >12 h, respectively (see Supplementary Figs. S1–S7 and Supplementary Tables S1–S6 for details). Since the heating conditions determine the chemical composition of the obtained product, the relationship between the heating temperature and S content in α-$Zr_2SP_2O_{12}$ was investigated (Fig. 1b). After heating at temperatures below 723 K, the value of 2S/Zr was >1 (the stoichiometric composition of α-$Zr_2SP_2O_{12}$), and ZrP_2O_7 was identified as an additional phase in the PXRD pattern (Fig. 1c). This indicates that the reaction temperature was not sufficient to obtain a single phase, resulting in unreacted sulfuric acid. After heating at 723 K, the 2S/Zr value was ~1.0, corresponding to the stoichiometric composition of α-$Zr_2SP_2O_{12}$, and the PXRD pattern showed only α-$Zr_2SP_2O_{12}$ (Fig. 1c). Rietveld analyses of the synthesized α-$Zr_2SP_2O_{12}$ were performed based on the space group $R\bar{3}c$ (#167) in the trigonal crystallographic system. The refined crystallographic parameters and reliability factors are provided in the Supplementary information (Supplementary Fig. S8 and Supplementary Table S7). The theoretical density of α-$Zr_2SP_2O_{12}$ was calculated to be ~3.0 g/cm^3.

The amount of S in the synthesized powder decreased with increasing heating temperature, as shown in Fig. 1b. The samples with 2S/Zr ranging from 0.48 to 1 contained a single crystalline phase identified as $Zr_2SP_2O_{12}$. In contrast, the samples with 2S/Zr = 0.43 and 0.44 included a second phase, ZrO_2. To determine the solid solubility limit, the lattice constant was plotted as a function of 2S/Zr (Fig. 1d). The lattice constants of both the *a*- and *c*-axis changed proportionally as 2S/Zr increased from 0.48 to 1. This suggests that the Vegard law applies at 2S/Zr = 0.48–1 and that the obtained compound is single-phase α-$Zr_2S_{0.9}P_2O_{12-\delta}$. Thus, subsequent characterization and evaluation focused primarily on α-$Zr_2S_xP_2O_{12-\delta}$ ($x = 0.48$–1).

The morphology of α-$Zr_2S_xP_2O_{12-\delta}$ was observed by (Fig. 2). The particles with a stoichiometric composition (α-$Zr_2SP_2O_{12}$) exhibited cube-like shapes with dimensions of ~200–300 nm. This unique shape is attributed to the rhombohedral lattice of the space group $R\bar{3}c$ (#167)[24]. The FE-SEM micrographs of α-$Zr_2S_xP_2O_{12-\delta}$ ($x = 0.54$, 0.76, and 0.9) also show essentially cubic particles (Fig. 2). The similar shapes of the particles with different compositions are likely a result of the preparation method; the α-$Zr_2S_xP_2O_{12-\delta}$ particles with $x = 0.54$, 0.76, and 0.9 were heated at a temperature higher than the optimum temperature used to obtain stoichiometric α-$Zr_2SP_2O_{12}$

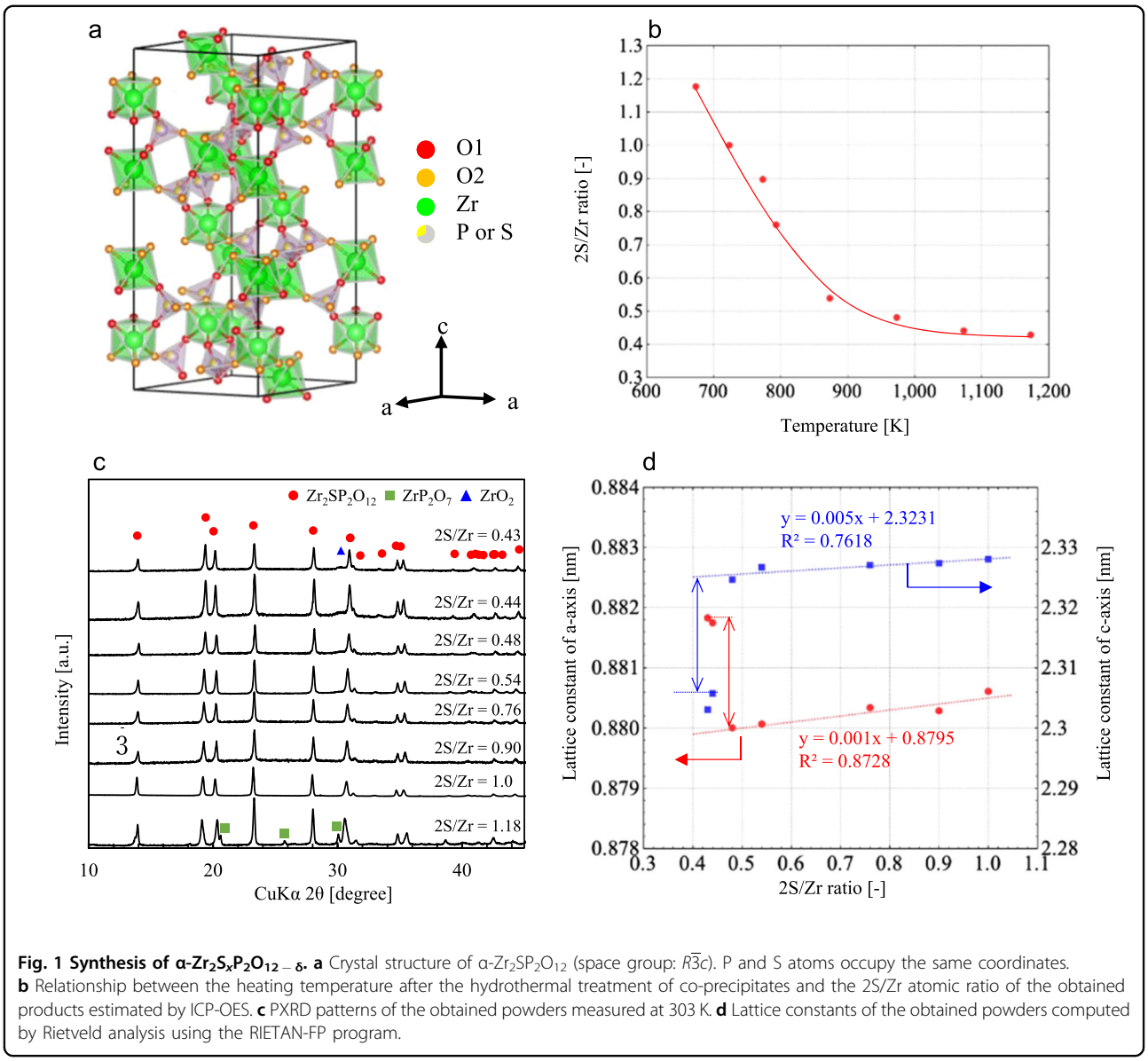

Fig. 1 Synthesis of α-$Zr_2S_xP_2O_{12-\delta}$. a Crystal structure of α-$Zr_2SP_2O_{12}$ (space group: $R\bar{3}c$). P and S atoms occupy the same coordinates. **b** Relationship between the heating temperature after the hydrothermal treatment of co-precipitates and the 2S/Zr atomic ratio of the obtained products estimated by ICP-OES. **c** PXRD patterns of the obtained powders measured at 303 K. **d** Lattice constants of the obtained powders computed by Rietveld analysis using the RIETAN-FP program.

particles. The cubic shape of α-$Zr_2SP_2O_{12}$ was formed during heating, and the S atoms were gradually released without deforming the particles at higher temperatures.

Thermal expansion behavior

To estimate the CTE, the lattice constants and volumes of the synthesized powders were calculated by Rietveld analysis based on the PXRD patterns measured at 303–773 K (Supplementary Fig. S9). Figure 3 shows the relationships between temperature and lattice constant and between temperature and lattice volume. The *a*-axis lattice constant of α-$Zr_2SP_2O_{12}$ remained nearly constant at 0.880 nm from 303 to 393 K and then increased to ~0.0883 nm from 393 to 453 K. At temperatures >453 K, the lattice parameter decreased slightly with increasing temperature. The *c*-axis lattice constant also remained constant from 303 to 393 K and then decreased greatly as the temperature increased from 393 to 453 K. Upon further increasing the temperature, the *c*-axis lattice constant increased slightly. Based on these results, the lattice volume decreased over the studied temperature range. The average-volume CTE, α_v, in the temperature ranges of 303–393, 393–453, and >453 K were −14.4, −70.0, and −27.4 p.p.m./K, respectively. The S-deficient compound α-$Zr_2S_xP_2O_{12-\delta}$ showed the same tendency; however, α_v became more pronounced. The calculated values of α_v are summarized in Table 1. The minimum α_v value of −108 p.p.m./K was observed for α-$Zr_2S_{0.9}P_2O_{12-\delta}$ at 393–453 K; this compound exhibited a volume reduction of ~1.3% from 303 to 773 K. As mentioned above, the CTE of

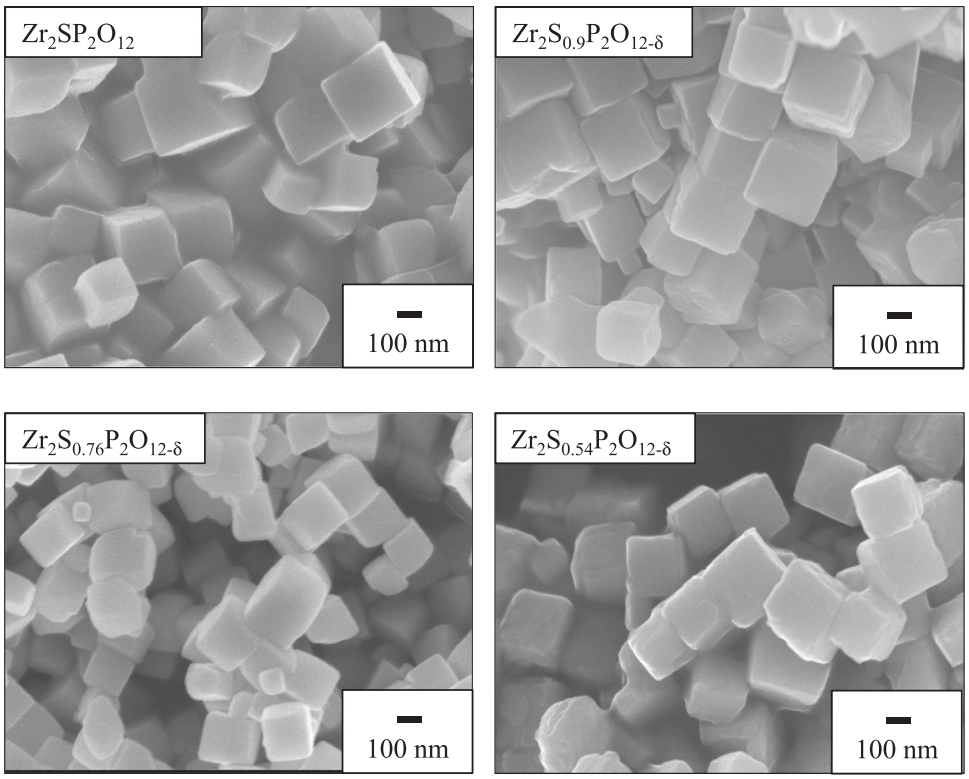

Fig. 2 FE-SEM micrographs of the obtained α-$Zr_2S_xP_2O_{12-\delta}$ powders. Chemical composition was determined by ICP-OES.

α-$Zr_2SP_2O_{12}$, with the space group $R\bar{3}c$, is lower than that of other materials, such as $Sc_2W_3O_{12}$, with the space group *Pbcn* ($\alpha_v = -6.5$ p.p.m./K)[25], and $ZrMgMo_3O_{12}$, with the space group $Pna2_1$ ($\alpha_v = 0.5$ p.p.m./K)[17].

Incidentally, good reproducibility of the above lattice constant changes was observed. The lattice volume obtained by high-temperature XRD was almost the same for both heating and cooling (Supplementary Fig. S10). Moreover, the chemical composition, determined by ICP-OES analysis, before and after the experiment confirmed that the material had not decomposed. First, α-$Zr_2SP_2O_{12}$ was synthesized by heating at >723 K.

Discussion

The mechanism of the observed negative thermal expansion was evaluated using DSC experiments (Fig. 4a). The DSC results indicated a small endothermic peak at ~430 K, corresponding to the significant shrinkage observed in Fig. 3. This shrinkage is thought to originate from a phase transition. However, the data suggest an enthalpy of ~−3.6 mJ/mol, much smaller than the phase transition enthalpies of typical ceramics (e.g., ~−35 J/mol for the tetragonal-to-monoclinic phase transition of ZrO_2)[26].

To confirm the phase transition, changes in atomic coordination were estimated using the Rietveld method based on the PXRD patterns (Supplementary Tables S8–18) and visualized in VESTA 3[27]. First, the space group of α-$Zr_2SP_2O_{12}$ in the temperature range of 303–773 K was determined to be $R\bar{3}c$, indicating that the space group was not affected by the phase transition. Second, the changes in atomic coordination were explained by the temperature dependencies of the bond angles and lengths. Figure 4b shows the relationship between temperature and the Zr–O–P (S) bond angles (i.e., the bond angles between the ZrO_6 octahedral units and the PO_4 or SO_4 tetrahedral units). The Zr–O1–P and Zr–O2–P bond angles were estimated separately since the oxygen atoms occupy two positions (O1 and O2), as shown in Fig. 1a. At temperatures <413 K, the Zr–O1–P bond angle remained nearly constant at ~151.1°. When the temperature exceeded 413 K, the temperature of significant shrinkage in Fig. 3, both bond angles increased with increasing temperature. At temperatures above 413 K, both bond angles increased slightly with increasing temperature. In contrast, the Zr–O2–P bond angle increased with increasing temperature throughout the temperature range evaluated in this study. This bond angle showed a very large change in the temperature range where significant volume shrinkage occurred. Next, the deformation of the ZrO_6 octahedron was evaluated based on the O1–Zr and O2–Zr bond lengths (Fig. 4c). At temperatures below 400 K, the O2–Zr

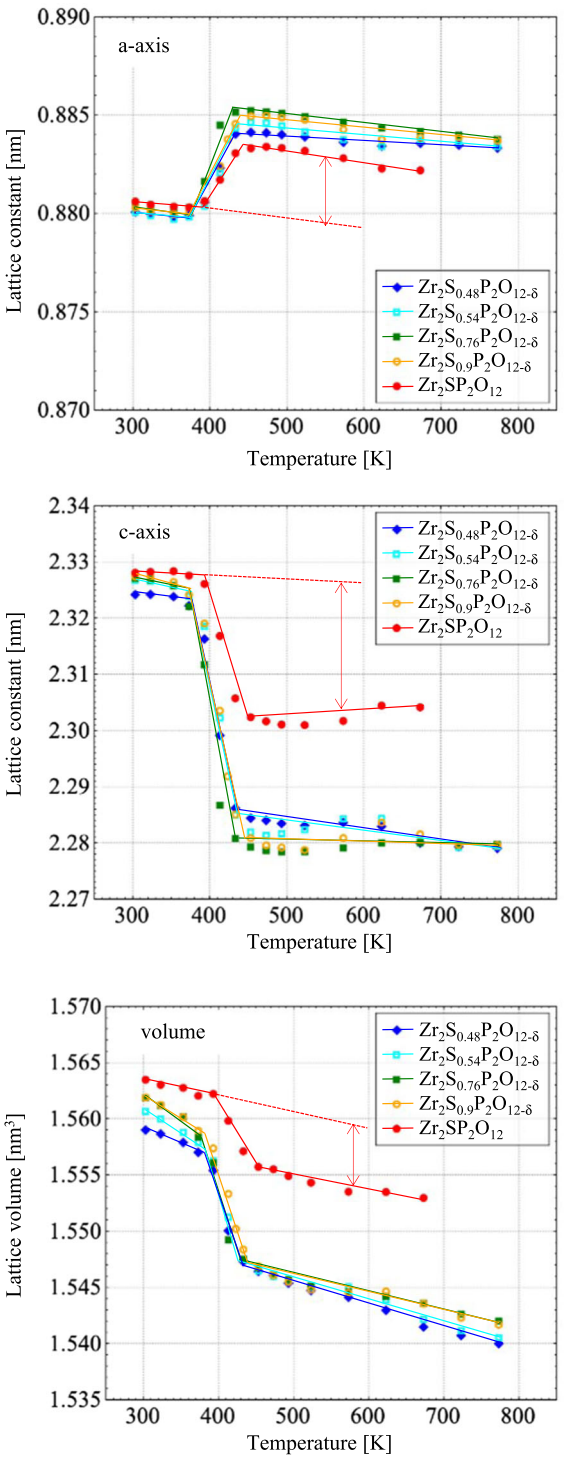

Fig. 3 Lattice constants and lattice volume change of α-$Zr_2S_xP_2O_{12-\delta}$ as a function of temperature. The upper and middle graphs shows lattice constant of a-axis and c-axis, respectively. The lower graphs shows Lattice volume. These were calculated using the Rietveld method (shown in Supplementary Fig. S9).

Table 1 CTE values calculated from high-temperature PXRD.

	α_v (p.p.m./K)		
	303–393 K	393–453 K	>453 K
α-$Zr_2SP_2O_{12}$	−14	−70	−27
α-$Zr_2S_{0.9}P_2O_{12-\delta}$	−26	−108	−9
α-$Zr_2S_{0.76}P_2O_{12-\delta}$	−30.4	−101	−9
α-$Zr_2S_{0.54}P_2O_{12-\delta}$	−25	−101	−12
α-$Zr_2S_{0.48}P_2O_{12-\delta}$	−17	−94	−13

bond length was greater than the O1–Zr bond length, and both remained nearly constant. In the temperature range associated with the endothermic DSC peak, the O1–Zr bond length increased with increasing temperature, while the O2–Zr bond length decreased. As a result, the lengths of O1–Zr and O2–Zr interchanged. In contrast, the O1–P and O2–P bond lengths decreased slightly with increasing temperature, although they did not change as much as the O1–Zr bond length (Fig. 4d). This indicates that the PO_4 or SO_4 tetrahedron did not change significantly with temperature.

Based on the above results, the mechanism of negative thermal expansion in α-$Zr_2SP_2O_{12}$ can be summarized as follows. At temperatures <393 K or >453 K, the ZrO_6 octahedral and PO_4 (or SO_4) tetrahedral units are hardly deformed, while the Zr–O1–P and Zr–O2–P bond lengths increase with increasing temperature. Thus, the negative thermal expansion in these temperature ranges is based on a framework-type mechanism, specifically the rigid unit mode model[28–31]. In the temperature range where significant shrinkage was observed, remarkable deformation of the ZrO_6 octahedral unit occurred (Fig. 4e, f). Based on the DSC results and the unchanged space group at temperatures lower and higher than the temperature of the endothermic peak, this deformation represents an isosymmetric phase transition[32]. Thus, α-$Zr_2SP_2O_{12}$ exhibits both framework- and phase transition-type mechanisms. Moreover, the movement of all atoms in the α-$Zr_2SP_2O_{12}$ lattice during heating was visualized; the video shown in the Supplementary information indicates that the observed thermal shrinkage originates from both the framework- and phase transition-type mechanisms.

The CTE of α-$Zr_2S_xP_2O_{12-\delta}$ changed based on the value of x. In particular, a significant decrease occurred in the temperature range around the isosymmetric phase transition. For the stoichiometric composition (α-$Zr_2SP_2O_{12}$), the ZrO_6 octahedral unit connects to two SO_4 tetrahedral

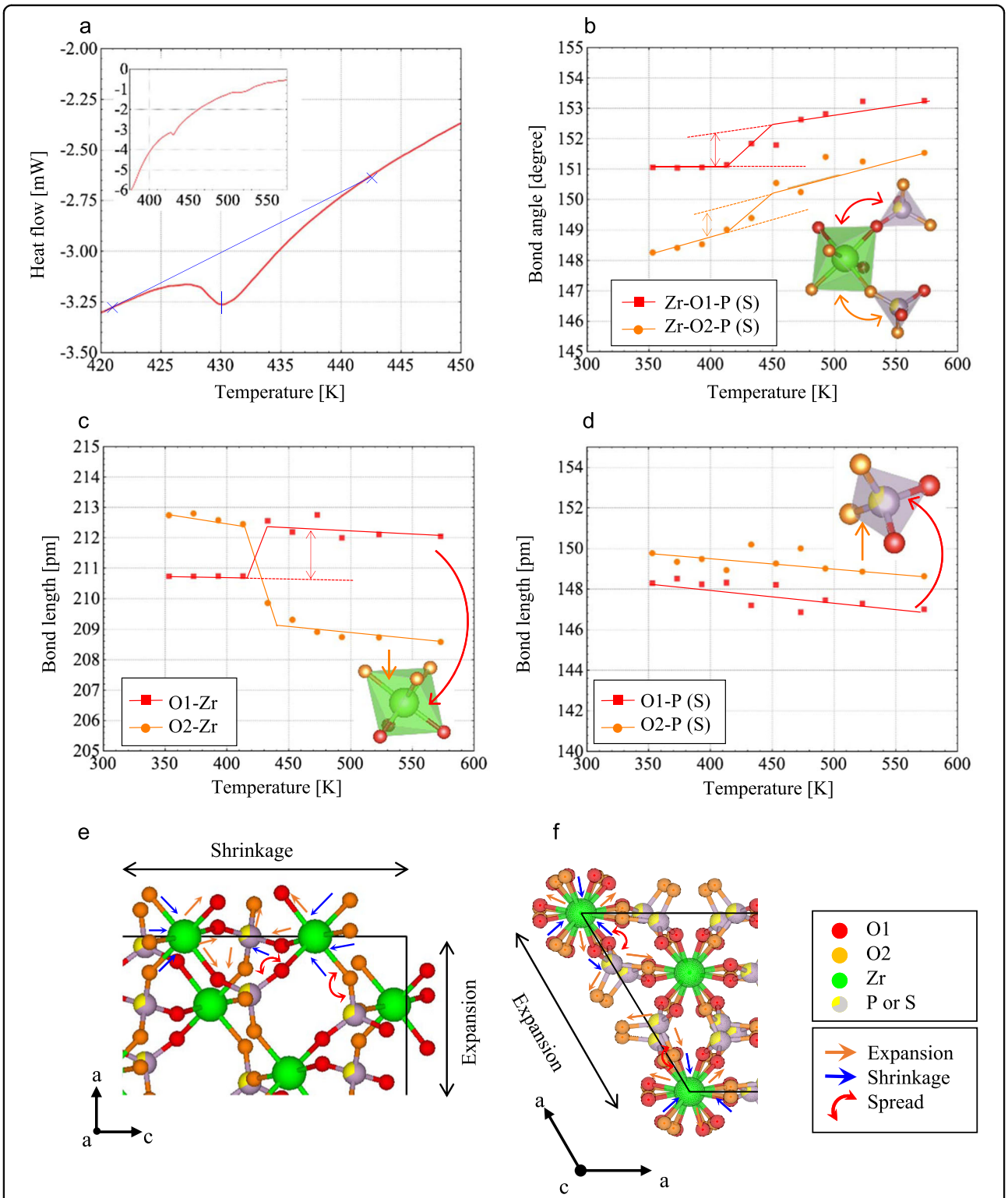

Fig. 4 Mechanism of negative thermal expansion. a DSC curve of α-$Zr_2SP_2O_{12}$. **b** Zr–O–P (or S) bond angle as a function of temperature. Atomic distances between **c** O atoms and Zr atoms, **d** O atoms and P (or S) atoms, and **e** Zr atoms as functions of temperature. Crystal structure of α-$Zr_2SP_2O_{12}$ viewed along the **e** *a*-axis and **f** *c*-axis. The P and S atoms occupy the same coordinates and cannot be distinguished.

and four PO_4 tetrahedral units. A small number of defects in the S tetrahedral unit affect the deformation of the ZrO_6 octahedral unit, contributing to the large deformation of the entire lattice. It is believed that S defects are formed in the crystal structure, which leads to easy deformation.

Acknowledgements
We are grateful to the Ookayama Materials Analysis Division of the Tokyo Institute of Technology for PXRD measurements, FE-SEM observations, and chemical composition estimation by ICP-OES. We thank Professor Hitoshi Kawaji and Katsumi Suda of the Tokyo Institute of Technology for critical advice on the phase transition.

Author contributions
T.I., Y.H., Y.A., R.U., S.M., and A.N. designed the study. T.I., Y.H., Y.A., and R.U. performed the experiments and analyzed the data. Y.H. and T.I. wrote the paper.

Conflict of interest
The authors declare that they have no conflict of interest.

Supplementary information is available for this paper at https://doi.org/10.1038/s41427-020-00266-9.

Received: 21 November 2019 Revised: 28 September 2020 Accepted: 5 October 2020.
Published online: 18 December 2020

References

1. Barrera, G. D., Bruno, J. A. O., Barron, T. H. K. & Allan, N. L. Negative thermal expansion. *J. Phys. Condens. Matter* **17**, R217–R252 (2005).
2. Miller, M., Smith, C. W., Mackenzie, D. S. & Evans, K. E. Negative thermal expansion: a review. *J. Mater. Sci.* **44**, 5441–5451 (2009).
3. Jakubinek, M. B., Whitman, C. A. & White, M. A. Negative thermal expansion materials: thermal properties and implications for composite materials. *J. Therm. Anal. Calorim.* **99**, 165–172 (2010).
4. Takenaka, K. Negative thermal expansion materials: technological key for control of thermal expansion. *Sci. Technol. Adv. Mater.* **13**, 013001 (2012).
5. Chen, J., Hu, L., Denga, J. & Xing, X. Negative thermal expansion in functional materials: controllable thermal expansion by chemical modifications. *Chem. Soc. Rev.* **44**, 3522–3567 (2015).
6. Dove, M. T. & Fang, H. Negative thermal expansion and associated anomalous physical properties: review of the lattice dynamics theoretical foundation. *Rep. Prog. Phys.* **79**, 066503 (2016).
7. Isobe, T. et al. Preparation and properties of $Zr_2MoP_2O_{12}$ ceramics with negative thermal expansion. *Mater. Des.* **112**, 11–16 (2016).
8. Nabetani, K. et al. Suppression of temperature hysteresis in negative thermal expansion compound $BiNi_{1-x}Fe_xO_3$ and zero-thermal expansion composite. *Appl. Phys. Lett.* **106**, 061912 (2015).
9. Yamashina, N., Isobe, T. & Ando, S. Low thermal expansion composites prepared from polyimide and ZrW_2O_8 particles with negative thermal expansion. *J. Photopolym. Sci. Technol.* **25**, 385–388 (2012).
10. Zhang, Z. et al. Synthesis of $Zr_2WP_2O_{12}/ZrO_2$ composites with adjustable thermal expansion. *Front. Chem.* **5**, 105 (2017).
11. Yanase, I., Sakai, H. & Kobayashi, H. Fabrication of $Zr_2WP_2O_{12}/ZrV_{0.6}P_{1.4}O_7$ composite with a nearlyzero-thermal-expansion property. *Mater. Lett.* **207**, 221–224 (2017).
12. Suzuki, T. & Omote, A. Zero thermal expansion in $(Al_{2x}(HfMg)_{1-x})(WO_4)_3$. *J. Am. Ceram. Soc.* **89**, 691–693 (2005).
13. Evans, J. S. O., Mary, T. A. & Sleight, A. W. Negative thermal expansion in a large molybdate and tungstate family. *J. Solid State Chem.* **133**, 580–583 (1997).
14. Isobe, T., Umezome, T., Kameshima, Y., Nakajima, A. & Okada, K. Preparation and properties of negative thermal expansion $Zr_2WP_2O_{12}$ ceramics. *Mater. Res. Bull.* **44**, 2045–2049 (2009).
15. Weck, P. F. et al. First-principles structural, mechanical, and thermodynamic calculations of the negative thermal expansion compound $Zr_2(WO_4)(PO_4)_2$. *ACS Omega* **3**, 15780–15788 (2018).
16. Cetinkol, M., Wilkinson, A. P. & Lee, P. L. Structural changes accompanying negative thermal expansion in $Zr_2(MoO_4)(PO_4)_2$. *J. Solid State Chem.* **182**, 1304–1311 (2009).
17. Romao, C. P. et al. Zero thermal expansion in $ZrMgMo_3O_{12}$: NMR crystallography reveals origins of thermoelastic properties. *Chem. Mater.* **27**, 2633–2646 (2015).
18. Mary, T. A. & Sleight, A. W. Bulk thermal expansion for tungstate and molybdates of the type $A_2M_3O_{12}$. *J. Mater. Res.* **14**, 912–915 (1999).
19. Roy, R., Agrawal, D. K., Alamo, J. & Roy, R. A. [CTP]: a new structural family of near-zero expansion ceramics. *Mater. Res. Bull.* **19**, 471–477 (1984).
20. Alamo, J. & Roy, R. Zirconium phospho-sulfates with $NaZr_2(PO_4)_3$-type structure. *J. Solid State Chem.* **51**, 270–273 (1984).
21. Izumi, F. & Momma, K. Three-dimensional visualization in powder diffraction. *Solid State Phenom.* **130**, 15–20 (2007).
22. Shi, X., Lian, H., Qi, R., Cui, L. & Yao, N. Preparation and properties of negative thermal expansion $Zr_2P_2WO_{12}$ powders and $Zr_2P_2WO_{12}$/TiNi composites. *Mater. Sci. Eng. B* **203**, 1–6 (2016).
23. Hayakawa, Y., Isobe, T., Matsushita, S. & Nakajima, A. Photocatalytic activity of $Zr_2(WO_4)(PO_4)_2$. *Ceram. Int.* **45**, 1430–1433 (2019).
24. Mohanty, D. et al. Synthesis and piezoelectric response of cubic and spherical $LiNbO_3$ nanocrystals. *RSC Adv.* **2**, 1913–1916 (2012).
25. Evans, J. S. O., Mary, T. A. & Sleight, A. W. Negative thermal expansion in $Sc_2(WO_4)_3$. *J. Solid State Chem.* **137**, 148–160 (1998).
26. Suresh, A., Mayo, M. J. & Porter, W. D. Thermodynamics of the tetragonal-to-monoclinic phase transformation in fine and nanocrystalline yttria-stabilized zirconia powders. *J. Mater. Res.* **8**, 2912–2921 (2003).
27. Momma, K. & Izumi, F. VESTA 3 for three-dimensional visualization of crystal, volumetric and morphology data. *J. Appl. Crystallogr.* **44**, 1272–1276 (2011).
28. Evans, J. S. O. Negative thermal expansion materials. *J. Chem. Soc. Dalton Trans.* **19**, 3317–3326 (1999).
29. Pryde, A. K. A. et al. Rigid unit modes and the negative thermal expansion in ZrW_2O_8. *Phase Transit.* **61**, 141–153 (1997).
30. Tao, J. Z. & Sleight, A. W. The role of rigid unit modes in negative thermal expansion. *J. Solid State Chem.* **173**, 442–448 (2003).
31. Wells, S. A., Dove, M. T., Tucker, M. G. & Trachenko, K. Real-space rigid-unit-mode analysis of dynamic disorder in quartz, cristobalite and amorphous silica. *J. Phys. Condens. Matter* **14**, 4645 (2002).
32. Christy, A. G. Isosymmetric structural phase transitions: phenomenology and examples. *Acta Crystallogr. B* **51**, 753–757 (1995).